Ionics (2020) 26:1379–1388
https://doi.org/10.1007/s11581-019-03249-1

ORIGINAL PAPER

Polycationic bimetallic oxide $CoGa_2O_4$ with spinel structure: dominated pseudocapacitance, dual-energy storage mechanism, and Li-ion hybrid supercapacitor application

Zheng-Hua He[1] · Jian-Fei Gao[1] · Ling-Bin Kong[1,2]

Received: 26 June 2019 / Revised: 16 August 2019 / Accepted: 1 September 2019 / Published online: 8 November 2019

Abstract

In this work, the polycationic bimetallic oxide $CoGa_2O_4$ with spinel structure was successfully prepared by simple hydrothermal and subsequent calcination methods. Following, half-cell electrochemical test showed that this material presented a hybrid energy storage mechanism, namely combining Ga alloying and Co_3O_4 conversion. The combination of the two energy story mechanisms makes $CoGa_2O_4$ have higher conductivity than other single metal oxides. According to the calculation of the relationship between peak current and sweep speed, the $b = 0.93$ of $CoGa_2O_4$ is obtained, and its electrochemical behavior is closer to capacitive behavior than that of Co_3O_4 and $NiCo_2O_4$. This makes it have excellent rate performance and cycle stability. Consequently, the $CoGa_2O_4$//AC Li-ion hybrid supercapacitor (LIHSC) device exhibits excellent cycling stability (capacity retention of 83% after 8000 cycles), high-energy density of 111.5 Wh kg^{-1} (at 100 W kg^{-1}), and high power density of 3927 W kg^{-1} (at 24 Wh kg^{-1}).

Keywords Dual-energy storage mechanism · Polycationic bimetallic oxide · Dominated pseudocapacitance · High electrical conductivity · Lithium-ion hybrid supercapacitor

Introduction

With the fast development of electronic equipment, fossil energy consumption and environmental pollution have become increasingly serious. It is particularly urgent to find new and renewable energy sources that can replace traditional fossil fuels that are effective ways to maintain the sustainable development of human beings [1, 2] among which Lithium-ion batteries and supercapacitors [3, 4] have been extensively studied, yet the low energy density of supercapacitors and lithium-ion batteries Low power density limits its wide range of applications. The electrochemical energy storage devices have attracted tremendous attention in the past decades due to renewable and environmentally friendly [5, 6]. So a new system, Li-ion hybrid supercapacitor (LIHSC), has gradually become a research hotspot due to that it combines the high-energy storage ability of LIBs and the high power delivery ability of supercapacitors [7]. The positive and negative electrodes with different energy storage mechanisms will provide different voltage windows for the charging and discharging process, which can broaden the operating voltage window of LIHSC, resulting in high-energy density [8]. However, battery-type anode materials kinetics based on the lithium ion intercalation and deintercalation is very sluggish, while capacitive cathode materials have a faster kinetic due to the adsorption/desorption of anions on their surfaces. The uncoordinated dynamics between cathode and anode make the performance of LIHSC not reach the ideal value. Therefore, it is of great significance to design and develop an anode material with fast charge transfer for LIHSC.

The performance of LIHSC mainly depends on the inherent charge storage capacity of electrode materials, especially

Electronic supplementary material The online version of this article (https://doi.org/10.1007/s11581-019-03249-1) contains supplementary material, which is available to authorized users.

✉ Ling-Bin Kong
konglb@lut.edu.cn

[1] State Key Laboratory of Advanced Processing and Recycling of Non-Ferrous Metals, Lanzhou University of Technology, Lanzhou 730050, People's Republic of China

[2] School of Materials Science and Engineering, Lanzhou University of Technology, Lanzhou 730050, People's Republic of China

anode materials. Therefore, the development, design, and synthesis of advanced battery electrode materials with high electrochemical performance have become the mainstream trend. Monometal oxides have been widely studied (NiO, Co_3O_4) due to their high theoretical capacity, but their low conductivity makes the charge transfer in Faradaic redox reaction slow and the rate performance is limited. However, the cathode is a capacitive material, and its adsorption and desorption processes are fast. This mismatch of anode and cathode dynamics limits the application of metal oxides in LIHSC. According to previous reports, pseudocapacitance is a Faraday process that takes place on the surface or the near surface, and its process is faster than the behavior of the battery [9]. Therefore, it is imperative to develop transition metal oxides with higher conductivity and dominated pseudocapacitance.

The anode materials of LIHSC are mainly carbon and transition metal oxide (TMO) electrode materials. According to the energy-storage mechanism of TMO anode materials, it can be divided into three types: (i) alloying-type materials. This material has a high specific capacity and a low lithiation potential (< 0.5 V, vs. Li/Li^+), but the significant volume expansion during charging and discharging seriously affects the structural integrity of the materials, leading to poor cyclic stability [10, 11]. (ii) A zero strain intercalation-type materials. As the anode material of LIHSC, it can improve the cyclic performance of the device. However, the relatively high lithiation potential (~ 1.6 V vs. Li/Li^+) and low capacity lead to poor energy density of the device [12]. (iii) A conversion-type material. For metal oxides, the volume change is small and the capacity is moderate during the lithiation process, but the lithiation potential is highly (1.0~1.5 V vs. Li/Li^+) [13].

At present, researchers have done a lot of work to optimize the electrochemical performance of anode materials. There are mainly the following three methods. Firstly, nanocrystallization of materials, which not only can provide buffer space to reduce volume expansion during charge and discharge but also increase electrode and electrolyte contact area [14–16]. Secondly, synthesis of bimetallic oxide, which two different metal elements have different expansion coefficients and redox potentials, which make the volume change gradually occur in the electrochemical process [17]. Another method is surface modification, which is by coating a conductive metal or conductive carbon-based material as a result of its surface modification, such as carbon coating, porous carbon, carbon nanotubes, graphene/graphite, and nickel foam [18, 19].

High capacity and wide potential window are important parameters to optimize the electrochemical performance of LIHSC. The low lithium intercalation potential of alloy materials ensures a wide potential window, and the conductivity is improved by combining with materials with different energy storage mechanisms. In recent years, spinel structured ternary transition metal oxides are widely studied due to their relatively high conductivity and more reactive sites, such as MCo_2O_4, MMn_2O_4, and MFe_2O_4 (M = Ni, Fe, Co, Mn, etc.). But, reports of gallium compounds are extremely rare. At present, bimetallic spinel oxide $CoGa_2O_4$ has been widely used in various fields because of its superior conductivity and higher electrochemical activity compared to monometal oxides [14], such as air-cathode catalyst in microbial fuel cells [20], electrode material in supercapacitors [21], and water oxidation [22]. But, over the years, this material has not been studied as the anode electrode material of lithium ion capacitor.

Inspired by this, self-assembly stack of $CoGa_2O_4$ sheet was accomplished by a facile hydrothermal process and followed by calcining. To the best of our knowledge, the synthesis of $CoGa_2O_4$ spinel structured bimetallic oxides was first applied to the electrochemical study of anode materials for LIHSC. $CoGa_2O_4$ has high conductivity, dominated pseudocapacitance, and combines different energy storage mechanisms, which makes it exhibit excellent performance in LIHSC. As a consequence, a high-performance LIHSC with a voltage of 4 V is prepared by combining with AC cathode and $CoGa_2O_4$ anode. The LIHSC shows an excellent energy density of 111.5 Wh kg^{-1} at a power density of 100 W kg^{-1} and power density of 3927 Wh kg^{-1} at an energy density of 24 W kg^{-1}. More remarkably, it displays about 83% capacity retention after 8000 cycles. The results show that a potential application of polycationic bimetallic oxide $CoGa_2O_4$ materials for LIHSC.

Results and discussion

The preparation of the self-assembly stack of $CoGa_2O_4$ sheet is schematically illustrated in Scheme 1 (experimental section for more details) [23]. In the first step, $Co(NO_3)_2{\cdot}6H_2O$ and $Ga(NO_3)_3{\cdot}XH_2O$ with a molar ratio of 1:2 were added to 70 ml distilled water, and then, a certain amount of NH_4F and CON_2H_4 were added to the above solution for stiring and hydrothermal reaction during the reaction process at 180 °C for 16 h. After the end of the reaction, cool to room temperature, wash three times with distilled water and ethanol, and then dry at 60 °C. Afterwards, in the second step, the obtained precipitates were calcined at 350 °C for 2 h in a N_2 atmosphere. After being cooled to room temperature,the $CoGa_2O_4$ was obtained. The high crystallinity and phase purity of as-prepared $CoGa_2O_4$ were confirmed by XRD [24]. Figure 1 a demonstrates that all of identified peaks of $CoGa_2O_4$ can be index to the standard cubic spinel structure $CoGa_2O_4$ phase (PDF#11-0698); the diffraction peaks observed at 2θ values of 18.430, 30.335, 35.749, 37.387, 43.432, 53.893, 57.445, 63.160, and 74.683 are indexed to (111), (220), (311), (222), (400), (422), (511), (440), and (533) crystal phanes [20]. No impurity diffrarction peak is detected,which shows the prepared samples form high purity and high crystalline phase [25].

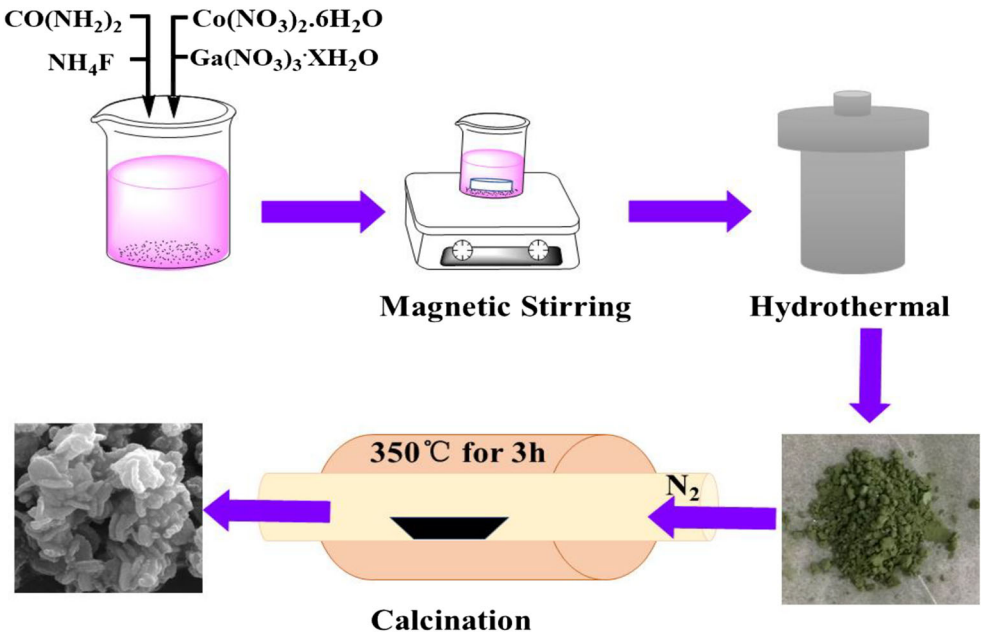

Scheme 1 Schematic of synthesis procedure of $CoGa_2O_4$

To further determine the element composition of $CoGa_2O_4$, an EDS analysis was carried out; the results of EDX analysi are consistent with Fig. 1b [26]. The result shows that the atomic percentages of Co and Ga are 13.47% and 25.32% respectively, indicating that the atomic ratio of Co and Ga is close to 1:2, which is in agreement with the expected stoichiometry of $CoGa_2O_4$ [21]. XPS was also performed in this experiment to further determine the constituent elements of $CoGa_2O_4$. By analyzing of the full spectrum of $CoGa_2O_4$ indicates the presence of cobalt, gallium, and oxygen (Fig. 1c) [27]. The peak of the binding energy around 300 eV is the peak of C1s, which may come from pollution. The remaining unmarked peaks are peaks of other valence states of Ga, such as Ga3s, Ga3p, Ga3d, and GaLMM [28]. The high-resolution Co2p sprctrum is given in Fig. 1d. The blinding energy at 796.864 eV and 780.819 eV is attributed to $Co2p_{1/2}$ and $Co2p_{3/2}$, which correspond to Co^{2+} state [21]. Other two peaks at 802.811 eV and 786.660 eV are identified as characteristic satellites (indicated as "Sat.") of Co2p [29]. The Ga 2p spectrum (Fig. 1e) is fitted well with Ga $2p_{3/2}$ and Ga $2p_{1/2}$ peaks at 1118.234 eV and 1145.065 eV, respectively [27]. The binding energy gap between the Ga $2p_{3/2}$ and Ga $2p_{1/2}$ states is 26.83 eV, which corresponds with the reference value of 26.84 eV. High-resolution O1s spectrum (Fig. 1f) is fitted by O1, O2, and O3 peaks. The O1 peak at 529.949 eV is indexed to typical metal–oxygen bonds; the O2 contribution at 531.025 eV is attributed to the defect sites with low oxygen coordination, contaminants, and surface species; and the O3 peak located at 532.407 eV is indexed to the multiplicity of physic- and chemi-sorbed water at or near the surface. Furthermore, the energy separation between the Co $2p_{3/2}$ and Ga $2p_{3/2}$ states (337.424 eV) indicates that the sample only contains the spinel $CoGa_2O_4$ phase and does not contain metal oxide powders such as CoO and Ga_2O_3 [21, 27, 30].

Figure 2 illustrates the morphology and structure of the $CoGa_2O_4$ investigated by scanning electron microscopy (SEM), transmission electron microscopy (TEM), and EDS mapping [8, 10]. Figure 2 a and b show the morphology of $CoGa_2O_4$; the large particles are formed by the aggregation of the $CoGa_2O_4$ sheet dun to their high specific surface area. Self-assembly stack of $CoGa_2O_4$ sheet increases the specific surface area and shortens the Li-ion diffusion. The TEM image (Fig. 2c) emerges that the prepared $CoGa_2O_4$ sample is sheet and piled up with each other, which forms lots of voids and is favorable for contact with electrolyte. The lattice fringes (Fig. 2d) are quite clear, revealing that the self-assembly stack of $CoGa_2O_4$ sheet is highly crystalline. The crystal plane spacing of lattice stripes is 0.2509 nm, which is consistent with the crystal plane spacing of (311) crystal planes of $CoGa_2O_4$ [31]. The blurry diffraction rings in selected-area diffraction (SAED) pattern of CoGa O indicate the polycrystalline nature and high crystallization properties of the material. In addition, selected area diffraction (SAED) pattern results of $CoGa_2O_4$ are consistent not only with XRD pattern (Fig. 1a) but also with previous literature reports [8, 21]. Figure 2 e shows the element distribution of Co, Ga, and O in the $CoGa_2O_4$ sample. It can be clearly seen from the figure that the three elements are evenly distributed [32]. In order to better analyze the performance of this electrode material, the N_2 adsorption-desorption isotherms of $CoGa_2O_4$ sample is presented in Figure S1a. Sheet $CoGa_2O_4$ material has a large specific surface area of 30.2 m^2g^{-1}. It can be seen from Figure S1b that the pores of the material are mainly composed of micropores and mesopores. The larger specific surface area and the presence of micro-mesoporous electrolyte make it easier to infiltrate and provide a beneficial channel for the transport of lithium ions.

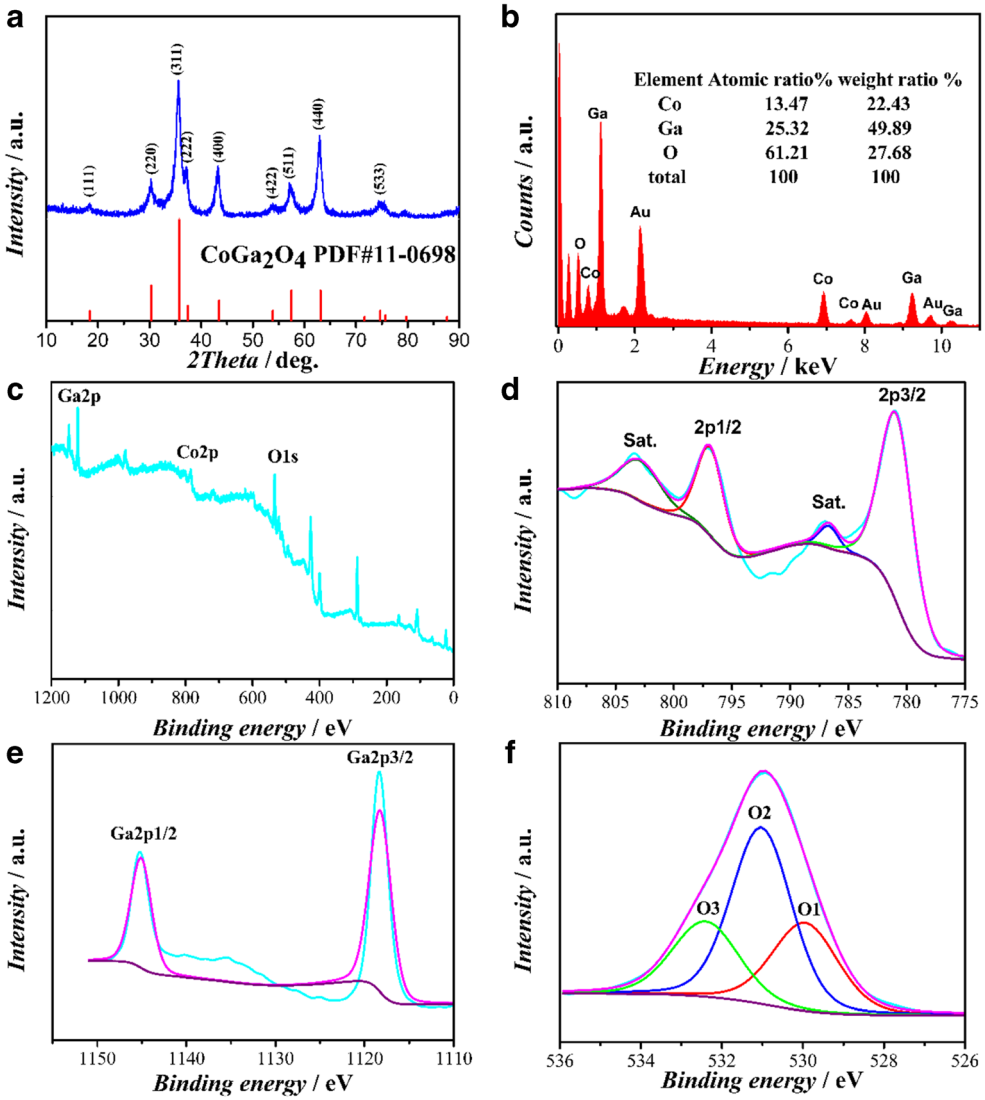

Fig. 1 XRD patterns, EDX spectrum, and XPS spectra of $CoGa_2O_4$. **a** XRD. **b** EDX. **c** Survey spectrum. **d** Co 2p. **e** Ga 2p. **f** O 1s

The electrochemical properties of the $CoGa_2O_4$ electrode were tested in a Li-ion battery with metallic lithium as the counter and reference electrodes. Figure 3 a shows the first three CV curves of $CoGa_2O_4$ electrode at a scanning rate of 0.1 mV s^{-1} between 0 and 3 V vs. Li^+/Li. The initial CV curve is completely different from the subsequent cycles, indicating that the reaction mechanism of the first cycles is different from that of the following cycles, which was owned to the decomposition of $CoGa_2O_4$ and irreversible reaction related to SEI film formation occurred in the first cycles [33]. In the first cathodic sweep, broad peak at 0.8 V could be assigned to the reduction of $CoGa_2O_4$ and the SEI film formation, which produced Co and Ga metals. In the subsequent cycles, the shape of the CV curve remained better, indicating a highly reversible lithiation/delithiation reaction. The complete overlapping of the shapes of the following two circles indicates that the cycle reversibility is better [34, 35]. During the cathodic scan, the large wide peak near 1 V is due to the oxidation process of Co^0 to Co oxides [36]. The peak at 0.3 V is assigned to the alloying reactions of Li_xGa. During the anodic scanning, a oxidation peak at closely 1 V attributed to the Li^+ dealloying from the Li_xGa alloy [37, 38]. According to the cyclic voltammogram test results, the electrode reaction process can be explained as follows [33, 37, 39]:

$$CoGa_2O_4 + 8Li^+ + 8e^- \rightarrow Co + 2Ga + 4Li_2O \quad (1)$$

$$Co + Li_2O = CoO + 2\,Li^+ + 2e \quad (2)$$

$$2Ga + 4Li^+ + 4e^- = 2Li_2Ga \quad (3)$$

Figure 3 b is the galvanostatic charging–discharging profiles of $CoGa_2O_4$ anode at current density of 0.1 A g^{-1}; the lithium intercalation potential of 0 to 0.5 V enables the LIHSC have a wide potential window(0–4 V). Figure 3 c further demonstrates the long cycle life of $CoGa_2O_4$; the initial capacity is 1476 $mAhg^{-1}$; it can be seen that the capacity is obviously

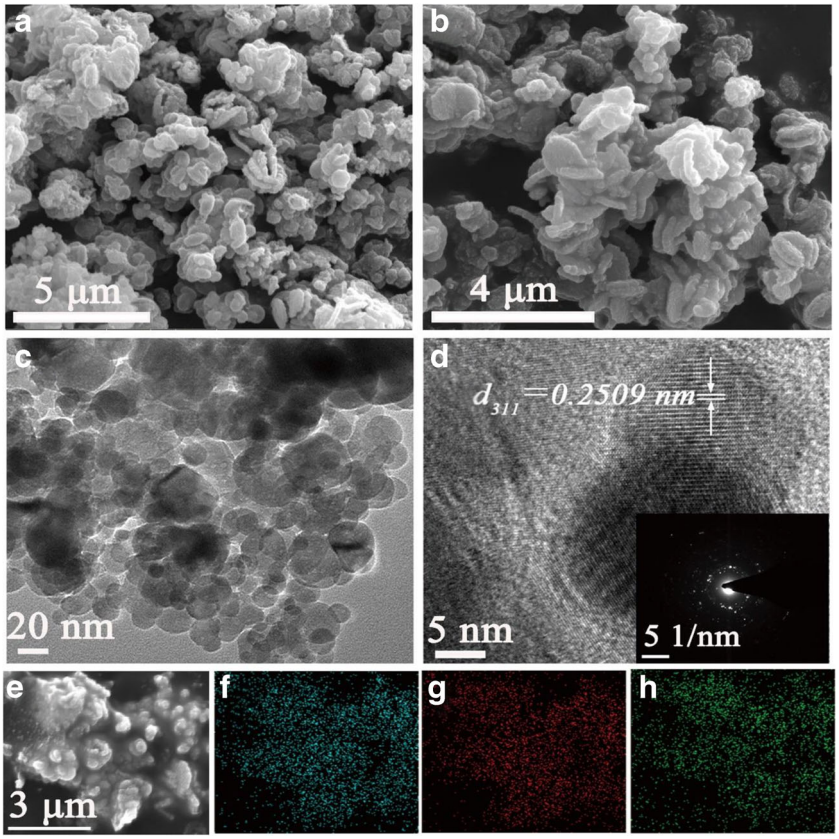

Fig. 2 SEM images, TEM images, HR-TEM images, SAED images, and mapping images of $CoGa_2O_4$. **a**, **b** The SEM pattern in × 10,000 and × 15,000, respectively. **c** TEM pattern. **d** The HR-TEM image over the crystallographic trait (inset: the SAED image). **e** EDS of $CoGa_2O_4$ and the corresponding element mapping: **f** Co, **g** Ga, and **h** O

attenuated from the first cycle to about 20 cycles; and finally, it delivers a capacity of 243 mAh g^{-1} after 200 cycles at the current density 0.1 A g^{-1} and the coulombic efficiency is close to 100%. The rapid capacity decline in the first 20 cycles may be due to the pulverization of electrodes, the detachment of active materials, and the collapse of the electrode material

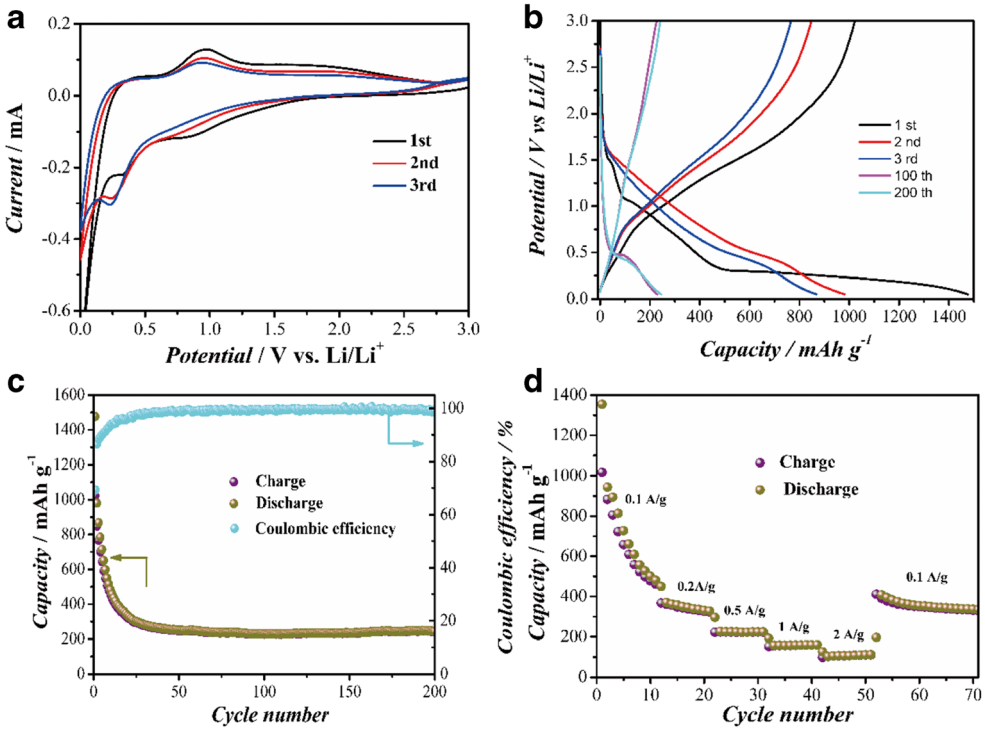

Fig. 3 **a** CV curves of $CoGa_2O_4$ at 0.1 mV s^{-1}. **b** Discharge–charge curves of the $CoGa_2O_4$ electrode at different number of cycles. **c** Long cycling performance of $CoGa_2O_4$ at the current density of 0.1 A g^{-1}. **d** Rate performance of $CoGa_2O_4$

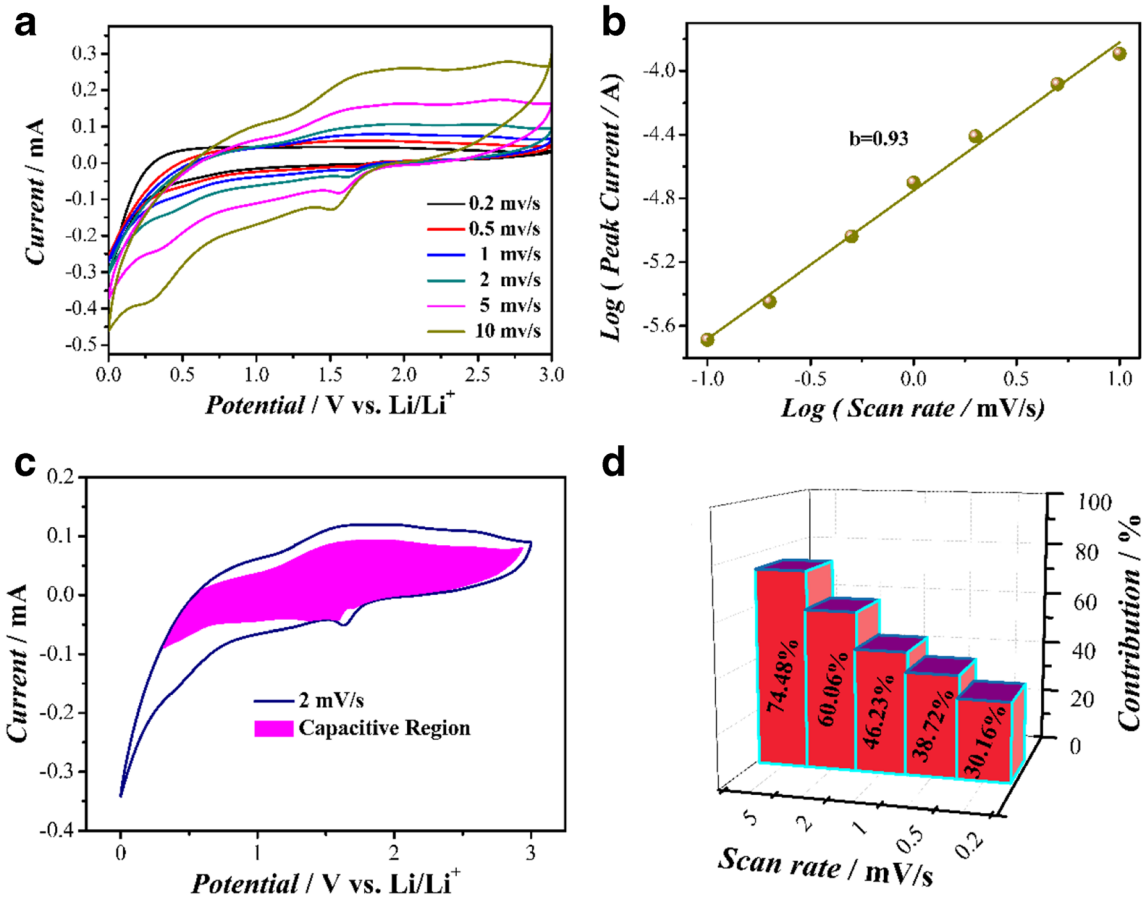

Fig. 4 Kinetics analysis of $CoGa_2O_4$. **a** CV profile of the $CoGa_2O_4$ anode at various scan rates of 0.2–10 mV s^{-1} in a potential range of 0–3.0 V. **b** specific peak current of $CoGa_2O_4$ at various sweep rates from 0.2 to 10 mV s^{-1}. **c** Capacitive contribution at 2 mV s^{-1} for the $CoGa_2O_4$ electrode. **d** Contribution ratio of the capacitive at different scan rates for the $CoGa_2O_4$ electrode

structure, which is due to the expansion of volume during the charge/discharge process. The rate capability of $CoGa_2O_4$ electrodes was investigated under galvanostatic charge–discharge at current densities from 0.1 to 2 A g^{-1} (Fig. 3d). When the current density increases from 0.1, 0.2, 0.5, 1, to 2 A g^{-1}, the corresponding discharge capacity is 400, 275, 200, 150, and 100 mAh g^{-1}. When returning to the 0.1 A g^{-1} test again, the corresponding discharge capacity reaches to 270 mAh g^{-1}. This indicates the excellent capacity reversibility of the $CoGa_2O_4$ anode. In order to more clearly explain the rapid attenuation of the capacity of $CoGa_2O_4$ electrode material in the first 20 cycles, after stable circulation, XRD and SEM of $CoGa_2O_4$ electrode material were tested under full charge. In Figure S2a, compared with standard PDF, Li_2O, Ga and Co materials exist, among which Ga_2O_3 and Co_3O_4 are caused by oxidation in the process of experiment and test. It can be seen from Figure S2b that in the charging and discharging process, the material structure is damaged and the electrode material becomes pulverized. This causes capacity to decay rapidly before 20 cycles and then stabilize.

In order to further explore the lithium storage kinetic of the $CoGa_2O_4$ electrode, CV profiles were carried out at scan rates of 0.2–10 mV s^{-1}, as exhibited in Fig. 4a. Moreover, the CV curves display similar shapes at different scanning rates, indicating advantageous reversibility [40]. To further explore the kinetics (Fig. 4b), it could be analyzed by plotting log(i) versus log(v) for cathodic or anodic peak currents. (The specific calculation is in the Supporting Information.) [41] The *b* value of cathodic peaks is 0.93 through calculation. It can be affirmed that the performance of Li-ion battery in $CoGa_2O_4$ presents intercalation mechanism dominated by pseudocapacitance, contributing to optimize the rate capability of anode materials [40]. In fact, the current response at a fixed potential consists of two parts: the current contributions of the pseudocapacitive effects and the diffusion-controlled Li^+ intercalation reactions [42]. This result may be related to the synergistic effect of dual-energy storage mechanisms of $CoGa_2O_4$. Dun et al. have explored and studied a method to study the material storage mechanism from CV curve, namely the capacitive behavior (k_1v) and diffusion control of Li ion intercalation ($k_2v^{1/2}$) [43, 44] (calculation formula is in the Supporting information). As shown in Fig. 4c, the shaded part is the contribution of pseudocapacitance at the scanning rate of 2 mV s^{-1}, accounting for 60.06% of the total. In order

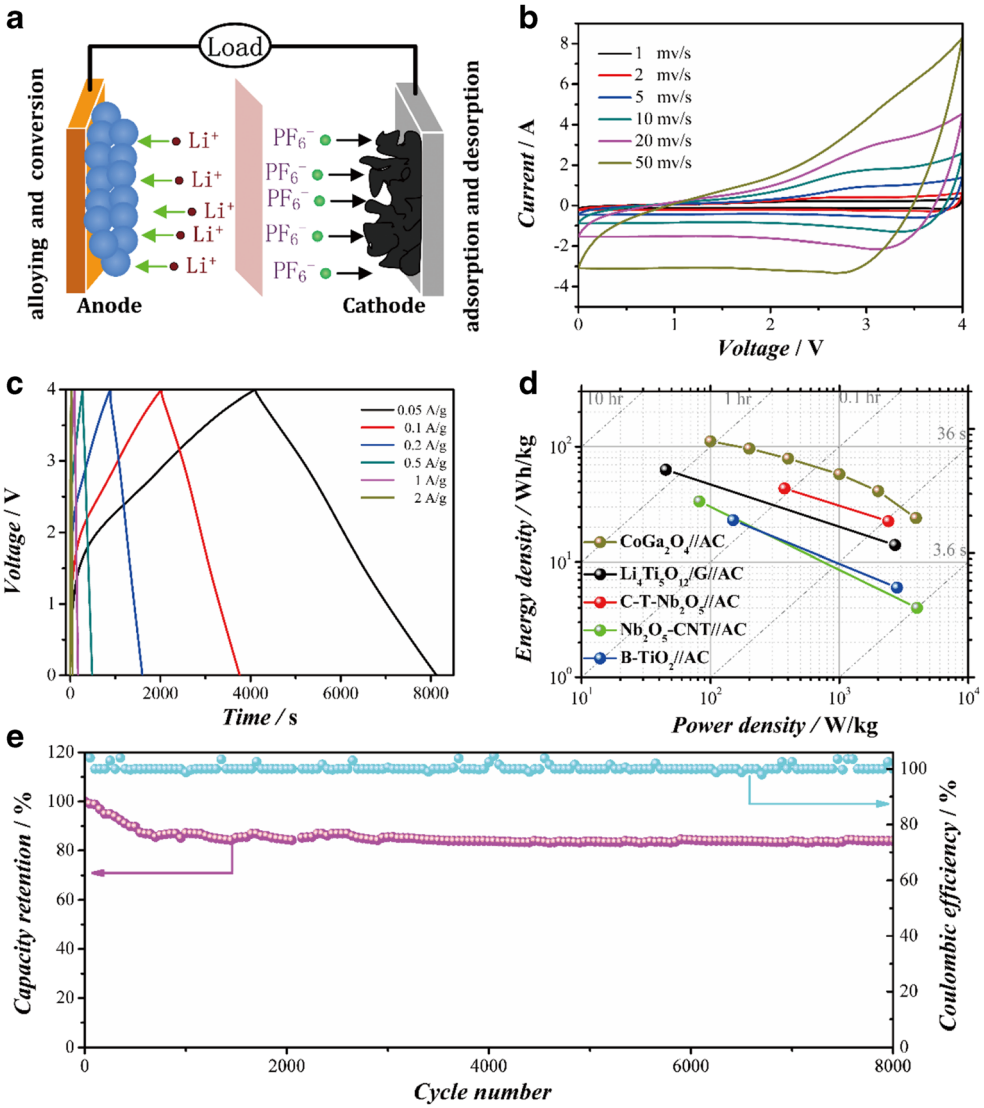

Fig. 5 **a** Schematic of the LIHSCs based on AC cathode and $CoGa_2O_4$ anode. **b** Curves of LIHSCs at different scan rates range from 1 to 50 mV s^{-1}. **c** Galvanostatic charge–discharge curves of LIHSCs at different current densities. **d** Ragone plot of LIHSCs. **e** long-term cycle performance of LIHSCs

to further explore the Li ion reaction kinetics of the $CoGa_2O_4$, capacitive contribution ratio scan rate plot is displayed in Fig. 4d. With the increase of scanning rate, the contribution ratio of capacitance gradually increases, indicating that the capacitance process dominates at high scanning speed. Based on the analysis and discussion of the above experimental results, it is concluded that the charge storage behavior of $CoGa_2O_4$ anode material is mainly carried out in the form of pseudocapacitance. Therefore, this material is suitable for LIHSC, effectively solves the problem of dynamic mismatch between positive and negative electrodes, and is conducive to rate performance and cycle stability. According to previous reports, the electrochemical kinetics process of Co_3O_4 and $NiCo_2O_4$ is dominated by diffusion control, which makes its rate performance less excellent than $CoGa_2O_4$ [6, 45].

The AC electrode material was also electrochemical tested before the LIHC was assembled, and the specific capacity remained stable at 120mAh g^{-1} for 1000 cycles at current density of 0.1 A g^{-1} (Figure S2). Figure 5 displays the electrochemical performance of the $CoGa_2O_4$//AC LIHSC. As schematically depicted in Fig. 5a, this LIHSC is composed of utilizing the as-prepared $CoGa_2O_4$ as anode and commercial activated carbon as cathode with 1 M $LiPF_6$ electrolyte. In the process of charging, lithium ions are intercalated into the self-assembled and stacked pieces of $CoGa_2O_4$; in order to keep the electrolyte neutral, anions are adsorbed on the surface of activated carbon to form an electric double layer [7, 31, 46]. The potential window the Li-ion hybrid supercapacitor ranges is from 0 to 4 V, which is attributed to the alloying and conversion of Li^+ happened in the voltage range of 0.1 to 0.5 V. This will facilitate the energy output of LIHSC [47]. Figure 5 b displays CV curves for LIHSC at different scanning rates from 1 to 50 mV s^{-1}. The CV curve of the LIHSC has a certain deviation from the quasi-rectangular curve due to the synergistic effect of different charge storage mechanisms of the

$CoGa_2O_4$ anode and the AC cathode [48]. Figure 5 c is a charge–discharge curve of the LIHSC under different current densities, which showing an approximate isosceles triangle shape, because the pseudocapacitance dominates in the $CoGa_2O_4$ anode. The specific capacitance values of the LIHSC are 50.2, 43.3, 35.5, 26, 18.5, and 11 F g^{-1} at the current densities of 0.05, 0.1, 0.2, 0.5, 1, and 2 A g^{-1}, respectively. Figure 5 d is the Ragone plot of the LIHSC; energy densities and power densities were calculated according to Formulas (4) and (5):

$$E = \frac{1}{2}C(\Delta V)^2 \quad (4)$$

$$P = E/t \quad (5)$$

where C is mass specific capacitance, t is the discharge time, and ΔV is the potential window. As expected, the LIHSC showed a high-energy density of 111.5 Wh kg^{-1} at 100 W kg^{-1} and a high-power density of 3927 W kg^{-1} at 24 Wh kg^{-1} [49]. Furthermore, the LIHC in this work exhibits excellent energy density and power density, comparing with previous reports on LIHC, such as $Li_4Ti_5O_{12}$/G//AC [50], C-T-Nb_2O_5//AC [51], Nb_2O_5-CNT//AC [52], and B-TiO_2//AC [53]. Moreover, from Fig. 5e, the capacity retention rate approached 83% after a cycle of 8000 at 1 A g^{-1} as well as Coulombic efficiency approached 100%. These results show that spinel $CoGa_2O_4$ is a promising material for lithium ion capacitors [54].

Conclusion

The material $CoGa_2O_4$ exhibits excellent electrochemical performance because of the combination of two different energy storage mechanisms namely Ga alloying and Co_3O_4 conversion and the material $CoGa_2O_4$ which is close to capacitive behavior by calculating $b = 0.93$(typical pseudocapacitance). Consequently, sheet $CoGa_2O_4$ material delivers a high reversible capacity of 243 mAh g^{-1} at a current density of 0.1 A g^{-1} with excellent rate performance and cycling stability. The designed 4.0-V class $CoGa_2O_4$//AC LIHSC exhibits a maximum capacity of 50.2 F g^{-1}. The highest energy density of 111.5 Wh kg^{-1} at a power density of 100 W kg^{-1} and the highest power density of 3927 kW kg^{-1} at an energy density of 24 Wh kg^{-1} were achieved by $CoGa_2O_4$//AC LIHSC devices. Therefore, it is of great significance to develop a material with dual-energy storage mechanisms and dominated pseudocapacitance.

Funding information This work was supported by the National Natural Science Foundation of China (No. 51762031, No. 51971104).

References

1. Chen ZK, Lang JW, Liu LY, Kong LB (2017) Preparation of a NbN/graphene nanocomposite by solution impregnation and its application in high-performance Li-ion hybrid capacitors. RSC Adv 7: 19967–19975
2. Mao-Cheng Liu, Yan Xu, Yu-Xia Hu, Qing-Qing Yang, Ling-Bin Kong, Wen-Wu Liu, Wen-Jun Niu, Yu-Lun Chueh, (2018) Electrostatically Charged MoS/Graphene Oxide Hybrid Composites for Excellent Electrochemical Energy Storage Devices . ACS Applied Materials & Interfaces 10 (41):35571-35579
3. Zhuang Wang, Jianmin Gu, Siheng Li, Guang Cong Zhang, Jinling Zhong, Xiaoyong Fan, Deling Yuan, Shoufeng Tang, Debao Xiao, (2018) One-Step Polyoxometalates-Assisted Synthesis of Manganese Dioxide for Asymmetric Supercapacitors with Enhanced Cycling Lifespan. ACS Sustainable Chemistry & Engineering 7 (1):258-264
4. Jianmin Gu, Xiaoyong Fan, Xin Liu, Siheng Li, Zhuang Wang, Shoufeng Tang, Deling Yuan, (2017) Mesoporous manganese oxide with large specific surface area for high-performance asymmetric supercapacitor with enhanced cycling stability. Chemical Engineering Journal 324:35-43
5. Chen L, Chen L, Zhai W, Li D, Lin Y, Guo S, Feng J, Zhang L, Song L, Si P, Ci L (2019) Tunable synthesis of Li_xMnO_2 nanowires for aqueous Li-ion hybrid supercapacitor with high rate capability and ultra-long cycle life. J Power Sources 413:302–309
6. Ding R, Qi L, Wang H (2013) An investigation of spinel $NiCo_2O_4$ as anode for Na-ion capacitors. Electrochim Acta 114:726–735
7. Tang X, Liu H, Guo X, Wang S, Wu W, Mondal AK, Wang C, Wang G (2018) A novel lithium-ion hybrid capacitor based on an aerogel-like MXene wrapped Fe_2O_3 nanosphere anode and a 3D nitrogen sulphur dual-doped porous carbon cathode. Mater Chem Front 2:1811–1821
8. Chen Z, Li H, Lu X, Wu L, Jiang J, Jiang S, Wang J, Dou H, Zhang X (2018) Nitrogenated urchin-like Nb_2O_5 microspheres with extraordinary pseudocapacitive properties for lithium-ion capacitors. ChemElectroChem 5:1516–1524
9. Lukatskaya MR, Dunn B, Gogotsi Y (2016) Multidimensional materials and device architectures for future hybrid energy storage. Nat Commun 7:12647
10. Wang X, Bi X, Zheng S, Wang S, Zhang Y, Du H, Lu J (2018) High-rate performance and ultralong cycle life enabled by hybrid organic-inorganic vanadyl ethylene glycolate for lithium-ion batteries. Adv Energy Mater 8:1801978
11. Li B, Zheng J, Zhang H, Jin L, Yang D, Lv H, Shen C, Shellikeri A, Zheng Y, Gong R, Zheng JP, Zhang C (2018) Electrode materials, electrolytes, and challenges in nonaqueous lithium-ion capacitors. Adv Mater 30:1705670
12. Ma K, Jiang H, Hu Y, Li C (2018) 2D nanospace confined synthesis of pseudocapacitance-dominated MoS_2-in-Ti_3C_2 superstructure for ultrafast and stable Li/Na-ion batteries. Adv Funct Mater 28: 1804306
13. Wu L, Lang J, Zhang P, Zhang X, Guo R, Yan X (2016) Mesoporous Ni-doped $MnCo_2O_4$ hollow nanotubes as an anode material for sodium ion batteries with ultralong life and pseudocapacitive mechanism. J Mater Chem A 4:18392–18400
14. Han N, Chen D, Pang Y, Han Z, Xia Y, Jiao X (2017) Structural regulation of $ZnGa_2O_4$ nanocubes for achieving high capacity and stable rate capability as an anode material of lithium ion batteries. Electrochim Acta 235:295–303
15. Li Z, Li B, Yin L, Qi Y (2014) Prussion blue-supported annealing chemical reaction route synthesized double-shelled Fe_2O_3/Co_3O_4 hollow microcubes as anode materials for lithium-ion battery. ACS Appl Mater Interfaces 6:8098–8107

16. Liu B, Zhang J, Wang X, Chen G, Chen D, Zhou C, Shen G (2012) Hierarchical three-dimensional $ZnCo_2O_4$ nanowire arrays/carbon cloth anodes for a novel class of high-performance flexible lithium-ion batteries. Nano Lett 12:3005–3011
17. Zheng H, Xu S, Li L, Feng C, Wang S (2016) Synthesis of $NiCo_2O_4$ microellipsoids as anode material for lithium-ion batteries. J Electron Mater 45:4966–4972
18. Pu J, Liu Z, Ma Z, Wang J, Zhang L, Chang S, Wu W, Shen Z, Zhang H (2016) Structure design of $NiCo_2O_4$ electrodes for high performance pseudocapacitors and lithium-ion batteries. J Mater Chem A 4:17394–17402
19. Mo Y, Ru Q, Chen J, Song X, Guo L, Hu S, Peng S (2015) Three-dimensional $NiCo_2O_4$ nanowire arrays: preparation and storage behavior for flexible lithium-ion and sodium-ion batteries with improved electrochemical performance. J Mater Chem A 3:19765–19773
20. Liu D, Mo X, Li K, Liu Y, Wang J, Yang T (2017) The performance of spinel bulk-like oxygen-deficient $CoGa_2O_4$ as an air-cathode catalyst in microbial fuel cell. J Power Sources 359:355–362
21. Chen X, Chai H, Cao Y, Jia D, Liu A, Zhou W (2018) Excellent cycle life of electrode materials based on hierarchical mesoporous $CoGa_2O_4$ microspheres. Chem Eng J 354:932–940
22. Xu Z, Yan SC, Shi Z, Yao YF, Zhou P, Wang HY, Zou ZG (2016) Adjusting the crystallinity of mesoporous spinel $CoGa_2O_4$ for efficient water oxidation. ACS Appl Mater Interfaces 8:12887–12893
23. Zhao X, Zhao Y, Liu Z, Yang Y, Sui J, Wang HE, Cai W, Cao G (2018) Synergistic coupling of lamellar $MoSe_2$ and SnO_2 nanoparticles via chemical bonding at interface for stable and high-power sodium-ion capacitors. Chem Eng J 354:1164–1173
24. Jiao X, Hao Q, Xia X, Yao D, Ouyang Y, Lei W (2018) Boosting long-cycle-life energy storage with holey graphene supported $TiNb_2O_7$ network nanostructure for lithium ion hybrid supercapacitors. J Power Sources 403:66–75
25. Zhuang B, Guo Z, Chu W, Cao Z, Bold T, Gao Y (2018) Mesoporous carbon film inlaid with $Li_3V_2(PO_4)_3$ nanoclusters through delaying sol-gel method for high performance lithium-ion hybrid supercapacitors. Electrochim Acta 283:1589–1599
26. Gao JF, Zhang WB, Zhao ZY, Kong LB (2018) Solid-phase synthesis and electrochemical pseudo-capacitance of nitrogen-atom interstitial compound Co_3N. Sustainable Energy & Fuels 2:1178–1188
27. Liu S, Hui KS, Hui KN, Li HF, Ng KW, Xu J, Tang Z, Jun SC (2017) An asymmetric supercapacitor with excellent cycling performance realized by hierarchical porous $NiGa_2O_4$ nanosheets. J Mater Chem A 5:19046–19053
28. Chu X, Wang, Bai L, Dong Y, Sun W, Zhang W (2018) Trimethylamine and ethanol sensing properties of $NiGa_2O_4$ nanomaterials prepared by co-precipitation method. Sensors Actuators B Chem 255:2058–2065
29. Mo Y, Ru Q, Song X, Hu S, Guo L, Chen X (2015) 3-dimensional porous $NiCo_2O_4$ nanocomposite as a high-rate capacity anode for lithium-ion batteries. Electrochim Acta 176:575–585
30. Chen H, Li GD, Fan M, Gao Q, Hu J, Ao S, Wei C, Zou X (2017) Electrospinning preparation of mesoporous spinel gallate (MGa_2O_4; M=Ni, Cu, Co) nanofibers and their M(II) ions-dependent gas sensing properties. Sensors Actuators B Chem 240:689–696
31. Han C, Xu L, Li H, Shi R, Zhang T, Li J, Wong CP, Kang F, Lin Z, Li B (2018) Biopolymer-assisted synthesis of 3D interconnected Fe_3O_4@carbon core@shell as anode for asymmetric lithium ion capacitors. Carbon 140:296–305
32. Mo Y, Qiang R, Chen J, Xiong S, Guo L, Hu S, Peng S (2015) Three-dimensional $NiCo_2O_4$ nanowire arrays: preparation and storage behavior for flexible lithium-ion and sodium-ion batteries with improved electrochemical performance. J Mater Chem A 3:19765–19773
33. Huang Y, Ouyang J, Tang X, Yang Y, Qian J, Lu J, Xiao L, Zhuang L (2019) $NiGa_2O_4$/rGO composite as long-cycle-life anode material for lithium-ion batteries. ACS Appl Mater Interfaces 11:8025–8031
34. Li B, Feng J, Qian Y, Xiong S (2015) Mesoporous quasi-single-crystalline $NiCo_2O_4$ superlattice nanoribbons with optimizable lithium storage properties. J Mater Chem A 3:10336–10344
35. Ju Z, Ma G, Zhao Y, Xing Z, Qiang Y, Qian Y (2015) A facile method for synthesis of porous $NiCo_2O_4$ nanorods as a high-performance anode material for Li-ion batteries. Part Part Syst Charact 32:1012–1019
36. Liu Y, Mi C, Su L, Zhang X (2008) Hydrothermal synthesis of Co_3O_4 microspheres as anode material for lithium-ion batteries. Electrochim Acta 53:2507–2513
37. Tang X, Huang X, Huang Y, Gou Y, Pastore J, Yang Y, Xiong Y, Qian J, Brock JD, Lu J, Xiao L, Abruna HD, Zhuang L (2018) High-performance Ga_2O_3 anode for lithium-ion batteries. ACS Appl Mater Interfaces 10:5519–5526
38. Saint J, Morcrette M, Larcher D, Tarascon JM (2005) Exploring the Li–Ga room temperature phase diagram and the electrochemical performances of the Li_xGa_y alloys vs. Li. Solid State Ionics 176:189–197
39. Mondal AK, Su D, Chen S, Xie X, Wang G (2014) Highly porous $NiCo_2O_4$ nanoflakes and nanobelts as anode materials for lithium-ion batteries with excellent rate capability. ACS Appl Mater Interfaces 6:14827–14835
40. Yang D, Zhao Q, Huang L, Xu B, Nanjundan AK, Xiu SZ (2018) Encapsulation of $NiCo_2O_4$ in nitrogen-doped reduced graphene oxide for sodium ion capacitors. J Mater Chem A 6:14146–14154
41. Zhu Y, Yang L, Jian S, Chen Y, Gu H, Wei J, Zhen Z (2017) Fast sodium storage in TiO_2@CNT@C nanorods for high-performance Na-ion capacitors. Adv Energy Mater 7:1701222
42. Huang H, Kundu D, Yan R, Tervoort E, Chen X, Pan L, Oschatz M, Antonietti M, Niederberger M (2018) Fast Na-ion intercalation in zinc vanadate for high-performance Na-ion hybrid capacitor. Adv Energy Mater 8:1802800
43. Wang J, Polleux J, Lim J, Dunn B (2007) Pseudocapacitive contributions to electrochemical energy storage in TiO_2 (anatase) nanoparticles. J Phys Chem C 111:14925–14931
44. Brezesinski T, Wang J, Tolbert SH, Dunn B (2010) Ordered mesoporous α-MoO_3 with iso-oriented nanocrystalline walls for thin-film pseudocapacitors. Nat Mater 9:146–151
45. Li J, Li Z, Ning F, Zhou L, Zhang R, Shao M, Wei M (2018) Ultrathin mesoporous Co_3O_4 nanosheet arrays for high-performance lithium-ion batteries. ACS Omega 3:1675–1683
46. Xu J, Liao Z, Zhang J, Gao B, Chu PK, Huo K (2018) Heterogeneous phosphorus-doped WO_{3-x}/nitrogen-doped carbon nanowires with high rate and long life for advanced lithium-ion capacitors. J Mater Chem A 6:6916–6921
47. Li G, Yin Z, Guo H, Wang Z, Yan G, Yang Z, Liu Y, Ji X, Wang J (2019) Metalorganic quantum dots and their graphene-like derivative porous graphitic carbon for advanced lithium-ion hybrid supercapacitor. Adv Energy Mater 9:1802878
48. Muralee Gopi Chandu VV, Singh Rana PJ, Padma R, Vinodh R, Kim HJ (2019) Selective integration of hierarchical nanostructured energy materials: an effective approach to boost the energy storage performance of flexible hybrid supercapacitors. J Mater Chem A 7:6374–6386
49. Jin L, Gong R, zhang w x y, Zheng J, Zh X, Zhang C, Xia YY, Zheng JP (2019) Toward high energy-density and long cycling-lifespan lithium ion capacitor: a 3D carbon modified low-potential Li_2TiSiO_5 anode coupled with a lignin-derived activated carbon cathode. J Mater Chem A 7:8234–8244
50. Lu C, Wang X, Zhang X, Peng H, Zhang Y, Wang G, Wang Z, Cao G, Umirov N, Bakenov Z (2017) Effect of graphene nanosheets on electrochemical performance of $Li_4Ti_5O_{12}$ in lithium-ion capacitors. Ceram Int 43:6554–6562

51. Wang X, Yan C, Yan J, Sumboja A, Lee PS (2015) Orthorhombic niobium oxide nanowires for next generation hybrid supercapacitor device. Nano Energy 11:765–772
52. Wang X, Li G, Tjandra R, Fan X, Xiao X, Yu A (2015) Fast lithium-ion storage of Nb_2O_5 nanocrystals in situ grown on carbon nanotubes for high-performance asymmetric supercapacitors. RSC Adv 5:41179–41185
53. Aravindan V, Shubha N, Ling WC, Madhavi S (2013) Constructing high energy density non-aqueous Li-ion capacitors using monoclinic TiO_2-B nanorods as insertion host. J Mater Chem A 1:6145–6151
54. Jiao X, Hao Q, Xia X, Wu Z, Lei W (2019) Metal organic framework derived Nb_2O_5@C nanoparticles grown on reduced graphene oxide for high-energy lithium ion capacitors. Chem Commun 55: 2692–2695